

EVERYFLARE II: ROTATION PERIODS AND STARSPOT COVERAGE OF COOL ACTIVE STARS THROUGHOUT THE SPIN-DOWN PROCESS

WARD S. HOWARD¹, HANK CORBETT¹, NICHOLAS M. LAW¹, JEFFREY K. RATZLOFF¹, AMY GLAZIER¹, OCTAVI FORS^{1,2}, DANIEL DEL SER^{1,2}, JOSHUA HAISLIP¹

Draft version April 25, 2022

ABSTRACT

We measure photometric rotation periods and starspot amplitudes in Evryscope light curves for 113 cool stars selected to have strong flaring. The Evryscope array of small telescopes has observed all bright nearby stars in the Southern sky, producing two minute cadence light curves since 2016. Long-term, high-cadence observations allow detection of rare flare events and long-term periodic variability, and provide tools to probe the complex relationship between stellar rotation, starspots, and superflares. We detect precise rotation periods from 0.3487 to 104 days with a median period uncertainty of 0.0024 days. We observe sinusoidal amplitudes from 0.008 to 0.216 g' magnitudes. We fold the TESS light curves of each target to the Evryscope-detected period and compare rotational amplitudes. TESS amplitudes are less than or equal to Evryscope amplitudes. We compute the Rossby number (R_o) for each star, finding 25 of our flare stars to be fast rotators ($R_o < 0.04$), 55 to be intermediate-period rotators ($0.04 < R_o < 0.4$), and 33 to be slow rotators ($R_o > 0.44$). We measure the photometric starspot coverage of each flare star, and find a median spot coverage of 14% of the stellar hemisphere. We constrain the minimum surface magnetic field strength consistent with our flare energies and spot coverage fraction to be 500 G, with later-type stars exhibiting lower minimum field strengths than earlier-type stars. We observe a possible change in starspot coverage at intermediate periods. However, we do not conclusively confirm the increased activity of intermediate rotators seen in previous studies. We then split all rotators at $R_o \sim 0.2$ into $P_{Rot} < 10$ d and $P_{Rot} > 10$ d bins and confirm short-period rotators exhibit higher superflare rates, larger flare energies observed, and higher starspot coverage fractions than do long-period rotators, at p-values of 7.3×10^{-5} , 1.2×10^{-6} and 0.0097, respectively.

Keywords: low-mass, stars: flare, ultraviolet: planetary systems, ultraviolet: stars, surveys

1. INTRODUCTION

Stellar rotation and surface magnetic activity (e.g. surface field topology, starspots, and flares) are intrinsically related phenomena. Quickly-rotating young stars drive increased surface magnetic activity, while surface magnetism controls the spin-down of stellar rotation with age (Weber & Davis 1967; Kawaler 1988). Spin-down from angular momentum loss depends on the coupling of the field to the stellar wind, with complex fields resulting in orders-of-magnitude weaker coupling than dipole-dominant fields (e.g. Brown 2014; Garraffo et al. 2015, 2016, 2018). Directly measuring whether surface field topology is simple or complex is difficult and expensive, and has only been performed in detail for about 10^2 cool stars with well-constrained stellar rotation periods (Shulyak et al. 2017). However, measuring the surface magnetic activity levels of many stars at a range of rotation periods may indirectly probe magnetic topology throughout spin-down.

1.1. Stellar activity as a probe of spin-down

Large surveys of stellar rotation periods provide insight into the periods at which the magnetic field may change

from simple to complex topologies. Stellar rotation surveys find few cool stars with rotation periods between ten and seventy days, but many faster and slower rotators (e.g. Newton et al. (2016b, 2018); Oelkers et al. (2018)). The transition from the quickly-rotating phase to slowly-rotating phase is therefore thought to occur rapidly for cool stars (Newton et al. 2016b, 2018) due to a change in the state of the surface magnetic field and the sudden increased rate of mass and angular momentum loss (AML) that results (Brown 2014). High mass stars spin down earlier than low mass stars; many field-age M-dwarfs are still actively spinning down (Newton et al. 2016b). The surface magnetic activity throughout spin-down may therefore provide insight into the changing magnetic field and conditions governing AML.

Stellar activity (e.g. stellar flaring and starspot coverage) is well known to decrease as stars spin down with age (Ambartsumian & Mirzoyan 1975). It is hypothesized that increased stellar activity may be observed from cool stars with intermediate rotation periods as the surface magnetic field evolves from a simple into a complex topology (Mondrik et al. 2019). Two common photometric stellar activity measurements that may trace the evolution of the magnetic field are the minimum starspot coverage fraction and the amount of stellar flaring.

Starspots are often used to measure the stellar rotation period. Starspots are a form of stellar activity that appear on the photosphere of a star and are effects of the interior stellar magnetic dynamo. Starspots are cooler than the rest of the photosphere, resulting in a flux dif-

* E-mail: wshoward@unc.edu

¹ Department of Physics and Astronomy, University of North Carolina at Chapel Hill, Chapel Hill, NC 27599-3255, USA

² Dept. de Física Quàntica i Astrofísica, Institut de Ciències del Cosmos (ICCUB), Universitat de Barcelona, IEEC-UB, Martí i Franquès 1, E08028 Barcelona, Spain

ference between the spotted and non-spotted surfaces of a star (Berdyugina 2005). As the photosphere rotates, starspots often induce regular brightness variations in stellar photometry and line shifts in stellar spectra. The stellar rotation period may then be measured using the period of photometric variation in the light curve (e.g. Baliunas et al. 1996; Affer et al. 2012; Newton et al. 2016b; Oelkers et al. 2018).

The fraction of the stellar hemisphere covered by starspots, or starspot coverage fraction, decreases at long rotation periods for stars above the fully-convective mass limit, probing the evolution of the star’s surface magnetic field throughout spin-down (e.g. Hartman et al. 2011; McQuillan et al. 2014; Newton et al. 2016b; Notsu et al. 2019; Morris et al. 2019). Starspot coverage fractions are inferred from either the amplitude of rotational modulation in the light curve (Maehara et al. 2012; Shibata et al. 2013; Notsu et al. 2013, 2019), or comparing TiO bands in stellar spectra with simulated template spectra of the spot and star (Neff et al. 1995; O’Neal et al. 2004; Morris et al. 2019). Starspots are easily observed on low-mass stars because the amount of light blocked by spots creates a high-amplitude signal (McQuillan et al. 2014). Not all spotted stars will produce photometric rotation periods; rotational variation from spots is suppressed for spots at the poles and stars with spots evenly distributed across the entire stellar surface (Morris et al. 2019). For example, McQuillan et al. (2014) observe 80% of all cool stars to exhibit rotation in *Kepler*, with the remaining 20% likely displaying spot distributions evenly spread across the star or concentrated at the poles.

Stellar flares are another indicator of surface magnetism. Flares occur when the surface magnetic field re-connects, impulsively releasing electromagnetic radiation. Because flaring depends on stellar rotation, young stars emit more frequent and energetic flares than do older stars. Ilin et al. (2019) find decreased flaring of young stars within open clusters of greater age. Flaring also depends upon stellar mass due to the depth of the convective layer. Cool stars are often flare stars, even emitting frequent superflares (e.g. Paudel et al. 2018; Howard et al. 2019): extremely intense flares that release 10-1000X more energy than those seen from the Sun. As M-dwarfs age, both the flare occurrence rate and flare energy decrease (Davenport et al. 2019). Because flares are intimately connected with the surface field and depend on stellar rotation, it is hypothesized they may be useful in separating M-dwarfs with complex and simple fields. An increased flare rate from late M-dwarfs has been observed at intermediate rotation periods ($10 < P_{\text{Rot}} < 70$ d), supporting this hypothesis (Mondrik et al. 2019).

The two stellar activity measurements of starspot coverage and flaring are closely linked. The largest flare a star may emit is limited by the stored magnetic energy of the starspot group that produced it. By comparing the largest flare observed from each star and the starspot coverage fraction of that star, the stellar magnetic field strength may be constrained. This is because the surface magnetic field strength adjusts the conversion from starspot size to flare energy; the field must allow the observed flares given the observed spot sizes. Notsu et al. (2019) constrain the fields of solar-type rotators in *Kepler* from the largest observed flares and starspot coverage. Similarly, estimates may be made for the surface mag-

netic field strengths of cool rotators as they spin down. Combining a large sample of stellar flares and rotation periods allows estimates of their minimum surface magnetic fields to be tested against typical magnetic field strengths of cool stars (Shulyak et al. 2017).

1.2. Effects of spin-down on the detection and environment of planets

Spin-down alters not just the star’s properties, but also the detection and environment of any planets orbiting the star. Cool stars frequently host rocky planets in the habitable zone (Dressing & Charbonneau 2015). Due to the decreased size of the habitable zone, these orbit much closer to the star than is the case for Sun-like stars (Kopparapu 2013). The space weather environment consisting of stellar radiation and wind changes during spin-down (Cohen et al. 2014; Airapetian & Usmanov 2016), potentially altering planetary habitability. Sufficiently-frequent superflares (i.e. several per year) may completely photo-dissociate ozone and other atmospheric volatiles in Earth-like planetary atmospheres. As stars spin down, the danger from extreme UV radiation may decrease. Alternately, Alvarado-Gómez et al. (2018) find high-energy particles associated with coronal mass ejections (CMEs) may be trapped by strong magnetic fields of hundreds of Gauss; a weakened stellar field would cause more high-energy particles to escape.

Rotating starspots are a major source of correlated noise for M-dwarf radial velocity (RV) planet searches (Robertson et al. 2014) and planetary atmospheric characterization (Wakeford et al. 2019). An active region (AR) on the star may suppress convection in the photosphere, periodically shifting RV lines. Such activity has even lead to false-positive planet detections (Robertson et al. 2014). Planets orbiting in the HZ of early M-dwarfs are particularly affected as the planet orbital period and typical stellar rotation period of field-age stars are similar (Newton et al. 2016a; Vanderburg et al. 2016). Accurate rotation periods of late K and early M-dwarfs are necessary for the successful follow-up of rocky planets orbiting these stars.

1.3. Photometric surveys of rotating cool stars

Large numbers of photometric rotation periods of cool stars have been or are being catalogued by various space-based and ground-based surveys. Examples include 5257 *Kepler* (Borucki et al. 2010) K5 and later rotators (at least 80% of which are M1 or earlier) from McQuillan et al. (2014), at least 10^5 - 10^6 K5 and later rotators from the Transiting Exoplanet Survey Satellite (TESS; Ricker et al. 2014) estimated from Stassun et al. (2019); Zhan et al. (2019), ~ 800 K5 or later rotators in the Kilodegree Extremely Little Telescope (KELT; Pepper et al. 2003, 2007, 2012) from Oelkers et al. (2018), and 628 mid-to-late M-dwarf rotators from MEarth (Nutzman & Charbonneau 2008; Berta et al. 2012) (Newton et al. 2016b, 2018). While about 1-10% of late K-dwarfs and early M-dwarfs are flare stars, about 30% of mid-to-late M-dwarfs are flare stars (e.g. Yang et al. 2017; Günther et al. 2019; Howard et al. 2019). Cross-matching stars in each survey with rotation periods against stars with stellar flares therefore significantly reduces the sample size.

Most cool stars with measured rotation periods will come from TESS; $\sim 10\%$ of which will be flare stars.

TESS is searching for transiting exoplanets across the entire sky, split into 26 sectors. TESS observes each sector continuously in the red with four 10.5 cm optical telescopes for 28 days at $21''$ pixel $^{-1}$. Optimized to observe low-amplitude variation from all nearby cool stars, TESS will contribute the majority of fast and intermediate-period cool rotators. However, the TESS primary mission observes most stars for only 28 days, decreasing its ability to measure the periods of slow rotators. Furthermore, the uncertainties to the periods of intermediate and slow rotators obtained by TESS will be large (e.g. errors from approximately ~ 0.1 -to- ~ 1 days) compared to longer-duration observations. Long-term ground-based monitoring by MEarth, KELT, and other surveys measure accurate rotation periods of bright rotators, but few late K and early M-dwarfs.

1.4. *Probing spin-down with Evryscope-measured rotation periods and stellar activity*

The Evryscope (Law et al. 2015; Ratzloff et al. 2019a) observes all bright nearby stars across the Southern sky. The Evryscope is an array of twenty-two 60mm telescopes which simultaneously image the entire accessible sky at $13''$ pixel $^{-1}$. Thus far, Evryscope has produced 2-minute cadence light curves of 15 million sources, including light curves of $\sim 0.5 \times 10^5$ cool stars. Evryscope light curves of sufficiently high-amplitude and bright rotators allow detection of significantly longer rotation periods than from TESS data alone. While TESS observes each star for ~ 28 days in the red at high photometric precision, Evryscope observes each star at moderate precision for several years in the blue. Combined rotation periods in the blue and in the red allows not only better error analysis of the rotation rate for large numbers of field stars during spin-down, but also an estimate of the color-dependence of starspot modulation during this process. Long-term monitoring by Evryscope also confirms whether periodic brightness modulation seen in TESS is transient or stable over the course of multiple years to better inform RV follow-up efforts of planet candidates.

In this work, we focus on the subset of Evryscope rotation periods of previously-identified flare stars from Howard et al. (2019) to explore starspots, flare energies, and superflare rates during spin-down. This subset of the Evryscope data was selected from cool stars with 2-minute cadence light curves from both Evryscope and TESS, allowing a comparison of Evryscope and TESS rotation. Our stars are primarily late K and early-to-mid M-dwarfs, where new extremely-precise stellar rotation period measurements are exceptionally useful in dis-entangling stellar rotation from the orbital periods of HZ planets. Future work will further explore the combined flare rate and starspot coverage in both the TESS and Evryscope bands.

In Section 2 of this work, we describe the Evryscope, light curve generation, rotation period, starspot, and stellar flare observations. In Section 3, we describe the distributions of rotation periods, Rossby numbers, starspot amplitudes, starspot coverage fractions, and surface magnetic field constraints. We discuss the decrease in activity with rotation period, and describe a possible increase in starspot coverage at intermediate rotation periods. In Section 4, we give discussion of our results and conclude.

2. EVERYFLARE: ALL-SKY STELLAR ACTIVITY SEARCH

The EvryFlare survey is an ongoing comprehensive survey of stellar activity from all cool stars observed by Evryscope in the accessible Southern sky. Evryscope monitors large flares, stellar rotation periods, and starspot coverage from all nearby cool stars.

2.1. *Evryscope sample of cool stars with rotation periods and flares*

We search for rotation periods in our sample of flaring cool stars (i.e. K5-M4 dwarfs) from Howard et al. (2019). Although Evryscope observes $\sim 0.5 \times 10^5$ cool stars, 2-minute cadence light curves of only 4,068 cool stars were produced by both Evryscope and TESS in the first six TESS sectors. We selected only stars with both a high-cadence light curve in the blue (Evryscope) and in the red (TESS) in order to compare the flare amplitudes, flare energies, flare rates, rotation periods and amplitudes of rotation between these bands. Evryscope observed 575 large flares with a median energy of 10^{34} erg from the 284 flare stars. Of these, rotation was detected for 113 stars. These stars comprise the sample of active cool rotators in this work. Future work will explore a larger sample in both Evryscope and TESS.

2.2. *Evryscope observations*

As part of the Evryscope survey of all bright Southern stars, we discover many variable stars and rotating stars with starspots. The Evryscope is an array of small telescopes that simultaneously images 8150 square degrees and 18,400 square degrees in total each night on the sky. Evryscope observes at two-minute cadence in g' (Law et al. 2015), and is optimized for bright, nearby stars, with a typical dark-sky limiting magnitude of $g'=16$. Each night, Evryscope continuously monitors each part of the sky down to an airmass of two and at a resolution of $13''$ pixel $^{-1}$ for ~ 6 hours. The system accomplishes this by employing a “ratchet” strategy, tracking the sky for 2 hours at a time before ratcheting back into the initial position and continuing observations (Ratzloff et al. 2019a).

The Evryscope has already obtained 3.0 million raw images, which we store as ~ 250 TB of data. Evryscope images are reduced at real-time rates using a custom data reduction pipeline (Law et al. 2016; Ratzloff et al. 2019a). Each 28.8 MPix Evryscope image is calibrated using a custom wide-field astrometric solution algorithm. Background modeling and subtraction is carefully performed before raw photometry is extracted within forced-apertures at coordinates in an Evryscope catalog of 3M known source positions, including all stars brighter than $g'=15$, fainter cool stars, white dwarfs, and a variety of other targets. We then generate light curves across the Southern sky by differential photometry in small sky regions using carefully-selected reference stars and across several apertures (Ratzloff et al. 2019a). Systematics are partially removed by employing two iterations of the SysRem detrending algorithm (Tamuz et al. 2005).

We periodically regenerate the entire database of Evryscope light curves in order to incorporate observations obtained since the last update and to improve the photometric precision. At the time the data was analyzed for the present work, the Evryscope light curve

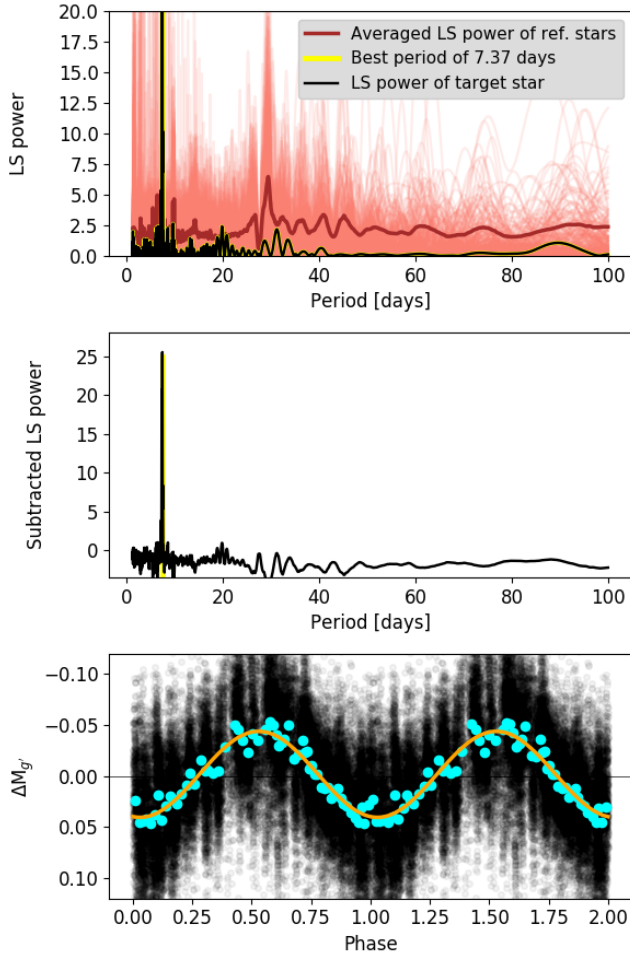


Figure 1. An example photometric rotation period found in an Evryscope light curve. The LS periodograms of all stars are plotted on top of each other in a transparent red color, while the “averaged” periodogram of the window function is plotted as a solid dark red line. The LS periodogram of the target star is plotted as a solid black line. The LS periodogram of the window function is then subtracted from the LS periodogram of the target star and searched for significant peaks, as displayed in the middle panel of Figure 1. The best period is highlighted in yellow. In the bottom panel, we plot $\Delta M_{g'}$ magnitudes versus phase. A folded and binned Evryscope light curve is plotted in blue points and compared to the best-fit sine in orange.

2.3. Evryscope rotation periods

We search for photometric rotation periods by computing the Lomb-Scargle (LS) periodogram (Lomb 1976; Scargle 1982; VanderPlas 2018) of each Evryscope light curve.

2.3.1. Initial detection of periods in Evryscope

We compute the LS power of each light curve for 10,000 frequency steps over a test period range of 1.25 to 100

days (and down to 0.1 days for select targets below). We usually exclude shorter periods because they are well-sampled by TESS (e.g. Zhan et al. (2019)). We subtract 27.5 day (likely lunar brightness variation) and 1 day best-fit sines from all light curves before computing the periodograms. LS power is reported in units of significance of detection, computed as the median-subtracted LS periodogram peak of the target star over the “noise” of the periodogram. We exclude a period region within 0.05 days of the detected peak from the noise computation.

In order to constrain systematics during the period analysis, we compare the LS periodogram of each target star with the combined LS periodograms of the other 283 flare stars in Howard et al. (2019), stepping through the entire sample star by star. Systematic behavior common to all light curves will increase the LS power of each star at systematics-affected periods. We therefore approximate the LS periodogram of our window function by averaging together the LS periodograms of all rotating and non-rotating stars, computing the median and standard deviation of the detected LS powers of all stars at each tested period. We define the LS periodogram of the window function as the 1σ upper limit of the distribution of LS powers at each tested period. This process is illustrated in the top panel of Figure 1.

The most-significant peak in the subtracted LS periodogram is selected as the best candidate period as shown in the middle panel of Figure 1. Candidate periods are investigated in a custom graphical user interface (GUI) by eye; the GUI is an interactive version of Figure 1. The light curve is folded to the period with the most significant peak and visually confirmed as a sinusoid. If the most significant peak is not a clear sinusoid, other significant peaks are inspected in the same way. The highest peak is sometimes a harmonic of the true rotation period or even a systematic in the light curve. If a clear sinusoidal signal can be detected, that period is recorded. Sometimes multiple real activity periodicities seem to be present- in such a case we record the most sine-like one from the visual inspection. The light curve of the target star is folded to the best-detected period in the bottom panel of Figure 1. If the LS power and oscillation amplitude are small and the power spectrum is noisy or dominated by systematic periods, we record no period for that target star. The best estimate for the period of each flare star is recorded in Table I of this work.

2.3.2. Bootstrap measurement of period uncertainty

Uncertainty to each Evryscope-detected period is computed with 200 trials of a custom bootstrap algorithm, which randomly drops 10% of the light curve before re-computing the LS periodogram. This method assumes a light curve that is much longer than the oscillation period, and tests if some small section of that light curve may unduly bias the recovered period. In each trial, periodograms are computed with 10,000 steps in frequency within 25% of the period previously confirmed by eye. Periods are tested as follows:

1. The bootstrap begins by searching in the periodogram for candidate peaks within 10% of the period previously confirmed by eye.

2. If the resulting periods do not converge to better than 10%, the period range of candidate peaks is extended and the bootstrap is re-run. This time, candidate peaks within 20% of the period previously confirmed by eye are allowed.
3. If the resulting periods do not converge to better than 20%, the bootstrap fails. The uncertainty to the period is reported to be greater than 20% and no further iterations are attempted for that target. Uncertainties larger than 20% are rare and generally occur only if the period selected by eye that best phases up the light curve is not the most significant peak in a narrow window in the periodogram.

2.3.3. Period validation using TESS light curve

As a further validation step, we fold the corresponding 2-minute cadence TESS light curve to our detected period. If we observe no coherent behavior at that period in TESS data, we record that information in Table 1. We note that a lack of TESS periodicity at our detected period does not mean our period is not astrophysical. Starspots evolve over time (Giles et al. 2017), may display a change in contrast against the star at different wavelengths (Notsu et al. 2019), and may even be altered by large flares (Zhan et al. 2019).

Many TESS SAP flux light curves demonstrate long term trends; to prevent these trends from altering TESS starspot amplitudes, we pre-whiten the light curves at timescales longer than the Evryscope-detected periodicity. We record whether the TESS light curve folds exactly to the Evryscope period in Table 1. If so, we also record the amplitude of the oscillation in TESS-magnitude and normalized flux in Table 1 for comparison to the Evryscope values. The folded TESS light curves that phase exactly to Evryscope periods are plotted against the folded Evryscope light curves in Figure 3.

While folding TESS light curves to the Evryscope period of each rotator identified by eye above, we discovered 27 of our rotation periods in the 1.25+ day range were aliases of an obvious rapid-rotator in TESS. As a result, we re-computed the LS periodogram of the Evryscope light curve down to 0.1 days for each star with likely aliasing due to rapid rotation. Out of 284 stars, we only re-computed periodograms for the 113 stars with previous rotation detected.

We may sometimes detect a period not evidenced in the TESS light curve or vice versa. Stars sometimes display periodicity at multiple periods (e.g. a binary with different-mass companions and different rotation periods superimposed on the light curve. For an example, see the panel in the third column in the second row of Figure 3). Also, systematics in the TESS light curve, in the Evryscope light curve, or in both may cause difficulty in comparing the two periods. In particular, uncorrected TESS systematics in multi-sector light curves may obscure periods of slow rotators.

2.4. Characterizing Stellar Parameters

Obtaining accurate values of stellar effective temperature and stellar radius helps constrain the physical pa-

rameters of starspots. All values are given for each star in Table 1.

2.4.1. Estimating Photometric Spectral Type

We estimate the photometric spectral type of each star. Because Howard et al. (2019) estimated spectral type from one color and a Gaia DR2 distance, we find the g' blue band may over-predict the stellar effective temperature of red dwarfs by several hundred K compared to classifiers that use several colors (e.g. Ratzloff et al. 2019b). To provide increased accuracy in our sub-type classification, we use the photometric spectral type classifier described in Ratzloff et al. (2019b).

Briefly, Ratzloff et al. (2019b) classifies main sequence dwarfs by their reduced proper motion (RPM) and multiple stellar colors using a Gaussian Mixture Model (GMM; Pedregosa et al. 2012). The GMM calculates the negative-log-likelihood and confidence level each star has been correctly classified. The GMM classifies M-dwarfs to within at least 3 spectral sub-types 95% of the time. While it is possible for an RPM classifier to fail to separate dwarf and giant stars at low RPM, we do not consider this to be a concern because the entire sample of stars was separately classified on the basis of Gaia DR2 parallax and APASS DR9 g-magnitude; we desire to increase the precision of sub-type measurements made from one color toward several colors. Out of 113 stars, the GMM classified 93 cool stars. For 18% of our stars, no classification was given, likely a result of having too few cross-matched colors or a very low RPM. For stars without a classification, we assign the spectral type via the absolute g-magnitude as described in Howard et al. (2019).

2.4.2. Estimating Stellar Effective Temperature, Mass, and Radius

We compute stellar **effective temperature** from the estimated spectral type using the relations given in Table 5 in the Appendix of Kraus & Hillenbrand (2007). We also compute stellar **mass** from the estimated spectral type using the relations given in Table 5 in the Appendix of Kraus & Hillenbrand (2007). We compute stellar **radius** using the mass-radius relationship for cool stars given in Mann et al. (2015).

2.5. Characterizing Starspots and Flares

Assuming that the observed sinusoidal stellar brightness variations are caused by star spots rotating into and out of view, we may investigate the nature of the star spots in our sample. For each rotating star in our sample, we may estimate the following starspot parameters:

- We estimate starspot temperature using the relationship between stellar effective temperature T_{eff} and starspot temperature T_{spot} from Notsu et al. (2019):

$$\Delta T(T_{\text{star}}) = T_{\text{star}} - T_{\text{spot}} = 3.58 \times 10^{-5} T_{\text{star}}^2 + 0.249 T_{\text{star}} - 808 \quad (1)$$

We note this fit was derived for solar type stars observed by *Kepler* and is extrapolated into the cool star regime. We therefore urge caution in the application of these values.

- We measure **spot coverage** as the starspot area A_{Spot} divided by the projected hemispherical area of the star A_{Star} . We use the relation described in Maehara et al. (2012); Shibata et al. (2013); Notsu et al. (2013, 2019):

$$\frac{A_{\text{Spot}}}{A_{\text{Star}}} = \frac{\Delta F}{F} \left[1 - \left(\frac{T_{\text{Spot}}}{T_{\text{Star}}} \right)^4 \right]^{-1} \quad (2)$$

$\Delta F/F$ is the normalized flux difference in brightness between the brightest part of the star and the dimmest side and is in units of fractional-flux. A_{Star} is given as $A_{\text{Star}} = \pi R_{\text{Star}}^2$. The bolometric spot area will differ from the spot area measured in a given bandpass.

These results and relevant uncertainties are displayed in Table 1 for each flare star. The measured rotation period and period error calculated as described in Section 2.3 is also included for each rotating flare star. The superflare rate, maximum flare energy, maximum flare amplitude, etc. from Table II of Howard et al. (2019) are also reproduced here in Table 1 for ease of reference.

2.6. Evryscope flare stars

The sample of large flares we employ in this work is the subset of flares from Howard et al. (2019) emitted from the rotating stars in Table 1. Flares are discovered and characterized as described in Howard et al. (2019). Briefly, we searched 2-minute cadence Evryscope light curves for large flares first by eye, and then with the Auto-ELFS automated flare-search algorithm.

The algorithm applies a flare matched-filter to the light curve and records brightening events that exceed the local noise by at least 4.5σ as flare candidates. Event start and stop times are determined by the first and last epochs to exceed the noise by 1σ around the peak epoch. The light curve of each flare candidate is converted to fractional-flux $\Delta F/F$ using the out-of-flare flux F_0 : $\Delta F/F = \frac{F - F_0}{F_0}$. The equivalent duration (ED) of each flare candidate is computed from the start to the stop time in seconds by a trapezoidal integration of the fractional-flux. We multiply the ED by the g' stellar quiescent flux (L_0) computed from the APASS DR9 (Henden et al. 2016) g' magnitude and Gaia DR2 (Gaia Collaboration et al. 2016, 2018) distance; L_0 is given in units of erg second^{-1} . Finally, we convert flare energies in g' to bolometric energies assuming a 9000 K flare blackbody. These events are inspected by eye for systematics or astrophysics other than flares as described in Howard et al. (2019) and subsequently confirmed or rejected.

We record flaring parameters for 284 flare stars in that work, including the maximum bolometric energy flare observed from each star during 2+ years of Evryscope observations, as well as the annual superflare rate of each star. We use here only these two flare star parameters to investigate the dependence of flaring upon stellar rotation and starspot coverage to avoid discovering random correlations between a large number of flaring variables.

3. STELLAR ACTIVITY AND ROTATION RELATIONS

We characterize stellar rotation, starspot coverage, and flare energy in the Howard et al. (2019) flare star sample.

3.1. Stellar rotation periods

We discover 113 stellar rotation periods out of 284 flare stars.

3.1.1. Distribution of detected periods

Periods detected in the Evryscope light curves range from 0.3487 days to 104 days with a median period and 1σ spread in the distribution of periods of 6.8_{-5}^{+34} days, as displayed in the left panel of Figure 4. Phase-folded light curves of a random subset of our detected rotation periods are displayed in Figure 2.

Because the Evryscope light curves are high-cadence and multi-year, the precision of many of our detected periods are good to 3-5 significant figures as displayed in the middle panel of Figure 4, with better precision for short periods than long periods. We detect all periods at significance levels greater than 5σ , as shown in the right panel of Figure 4, with greater significance for shorter periods.

3.1.2. Detection of Evryscope periods in TESS

During inspection of the TESS light curves of Section 2.3.3, we observe 69 periods clearly confirmed between the two surveys (shown in Figure 3), and 7 periods that are probably confirmed but do not clearly fold to the exact period detected by Evryscope, possibly due to spot evolution and differential rotation. 5 of our periods appear to be harmonics of the fundamental TESS period. Finally, 3 of our periods are too long to confirm in the TESS light curve. 28 of our periods do not correspond to any period in the TESS light curve.

3.2. Spot Coverage and Maximum Flare Energies

We measure a distribution of spot amplitudes ranging from 0.008 to 0.216 g' magnitudes, with a median amplitude and 1σ spread in the distribution of amplitudes of $0.033_{-0.014}^{+0.032}$ g' magnitudes, as shown in the left panel of Figure 5. We convert spot amplitude in g' magnitudes to the normalized peak-to-trough flux amplitude $\Delta F/F$, which may be understood as the fraction of starlight blocked by spots ($\Delta F/F$ is mathematically equivalent to fractional-flux). The median flux amplitude and 1σ spread in the distribution of normalized flux amplitudes is $0.061_{-0.026}^{+0.061}$ as shown in the middle panel of Figure 5.

The fraction of starlight blocked by spots $\Delta F/F$ is not equivalent to the hemispherical starspot coverage fraction $A_{\text{Spot}}/A_{\text{Star}}$. This is because starspot area depends on the temperature of the star and the temperature of the starspots as given in Equation 2. We estimate spot coverage fractions ranging from 0.03 up to nearly an entire stellar hemisphere; the median spot coverage fraction and 1σ spread in the distribution of spot coverage fractions is $0.14_{-0.07}^{+0.12}$. We note that coverage fractions depend on the assumed spot temperature, stellar radius, and fraction of bolometric spot flux observed in g' , which may each be in excess of 10% error; we urge readers to exercise caution in the use of these values where precision better than 50% is required.

Energy stored in starspots may be released in the form of stellar flares. The area of the smallest spot that could have produced a flare of bolometric energy E_{flare} is given

Table 1
Rotation Periods and Starspots on Cool Flare Stars Observed by Evryscope in TESS Sectors 1-6

TIC ID	Sector	RA	Dec	P _{Rot}	P _{Rot}	R _o	LS	Time of	EVR	EVR	Rot.	TESS	TESS	Spot	Mass	Rad.	T _{Eff}	SpT
		[J2018]	[J2018]	[d]	[d]		[σ]	peak	spot	frac.	in	TESS	frac.	temp.	[M _☉]	[R _☉]	[K]	
								phase	ampl.	light	TESS?	ampl.	blocked					
								[MJD]	[ΔM _J]	[ΔF/F]		[ΔM _J]	[ΔF/F]	[K]				
593228	5	71.84526	-27.8415	95.5	0.5	3.21	12	57751.049	0.013	0.024	no			3200	0.04	0.59	3800	M0
593230	5	71.84526	-27.8415	95.5	0.4	3.21	12	57751.049	0.013	0.024	no			3200	0.04	0.59	3800	M0
5656273	2	347.0817	-15.4098	0.43126	1e-05	0.01	57	58292.44	0.052	0.098	yes	0.018	0.035	3000	0.22	0.36	3400	M2.5
5796048	2	348.9343	-12.3647	0.5557	1e-05	0.01	33	57651.143	0.035	0.065	yes	0.016	0.031	3000	0.13	0.48	3600	M1.5
9210746	2	352.55716	-20.3916	7.482	0.005	0.12	14	57658.085	0.022	0.041	yes	0.006	0.011	2900	0.1	0.29	3400	M3
24662390	5	80.92147	-8.2824	13.4	0.7	0.49	9	58203.025	0.093	0.178	yes	0.019	0.039	3300	0.31	0.63	4100	K7
29853348	3	23.80831	-7.2144	0.70295	1e-05	0.01	33	57639.188	0.08	0.152	yes	0.048	0.096	2900	0.36	0.29	3400	M3
32811633	6	86.45644	-27.1606	49.5	1.2	1.12	16	57402.092	0.091	0.174	long			3000	0.37	0.42	3500	M2
33864387	most	65.41142	-72.5655	4.6133	0.0006	0.1	34	58143.255	0.04	0.075	yes	0.008	0.017	3000	0.16	0.42	3500	M2
43605290	5	75.48672	-6.9484	86.9	1.7	1.18	15	58075.161	0.052	0.098	harm.			2900	0.25	0.24	3300	M3.5
50745582	6	83.01872	-3.0913	3.74	0.01	0.06	11	57401.102	0.04	0.075	yes	0.011	0.022	2900	0.18	0.29	3400	M3
55368621	1-6	77.4463	-60.0016	45.1	0.1	1.65	16	57699.241	0.026	0.048	no	0.024	0.048	3000	0.24	0.42	3500	M2
71335815	1	331.21484	-47.5337	9.534	0.002	0.22	28	57610.053	0.054	0.101	yes	0.04	0.08	3000	0.08	0.63	4100	K7
77957301	5+6	79.34437	-35.3657	1.9254	0.0001	0.04	11	57746.101	0.017	0.031	prob.			3000	0.22	0.42	3500	M2
77959676	5+6	79.62111	-30.0256	1.6961	0.0001	0.06	25	57829.069	0.021	0.039	yes	0.006	0.013	3200	0.07	0.36	3400	M2.5
79566479	3+4	52.98208	-43.9871	2.9207	0.0003	0.1	27	57639.331	0.054	0.101	yes	0.029	0.058	3200	0.18	0.62	4000	K8
88479623	4	47.02903	-24.7596	0.459	1e-05	0.01	23	57992.327	0.009	0.017	harm.			3000	0.03	0.48	3600	M1.5
89205615	4	58.09812	-28.4386	0.3487	1e-05	0.01	13	57700.241	0.044	0.082	yes	0.016	0.031	3100	0.16	0.54	3700	M1
98796342	4	45.46199	-16.5934	104.0	1.6	2.73	12	58152.09	0.02	0.037	no			3000	0.08	0.48	3600	M1.5
98796344	4	45.46199	-16.5934	104.0	1.5	2.73	12	58152.09	0.02	0.037	no			3000	0.08	0.48	3600	M1.5
111184885	2	344.52609	-13.6438	18.0	0.5	0.64	9	57599.194	0.019	0.035	no			3200	0.06	0.62	4000	K8
115242300	2	6.269	-36.7714	12.7	0.007	0.2	19	57662.214	0.032	0.06	yes	0.008	0.017	2900	0.14	0.29	3400	M3
117874959	2	9.89891	-38.2837	6.314	0.003	0.09	28	57686.276	0.033	0.061	yes	0.034	0.067	2900	0.16	0.24	3300	M3.5
140045537	1	329.41269	-51.0094	1.12375	2e-05	0.01	34	57613.11	0.019	0.035	yes	0.004	0.007	2800	0.1	0.2	3200	M4
140045538	1	329.42117	-51.0075	1.12375	5e-05	0.02	47	57613.037	0.019	0.035	yes	0.004	0.007	2900	0.08	0.29	3400	M3
141807839	most	92.87476	-72.227	5.548	0.001	0.09	12	57657.272	0.049	0.092	no			2900	0.22	0.29	3400	M3

Notes. Parameters of 113 rotating flare stars monitored by Evryscope (1 star per row). This is a subset of the full table. The full table is available in machine-readable form, with extra columns on flare statistics repeated from matching rows in Table II of Howard et al. (2019). The columns here are: TIC ID, the TESS sector(s) the star was observed (if observed for more than 2 but less than six of the sectors, “most” is recorded), RA and Dec (the current Evryscope-measured positions of the star), the Evryscope-measured rotation period in days, the bootstrapped uncertainty on the Evryscope-measured period in days, the Rossby number, the significance of detection of the Lomb-Scargle significance in σ , a time of peak rotational brightness in the phase-folded Evryscope light curve, the Evryscope-measured starspot amplitude in ΔM_J , the Evryscope-measured starspot double-amplitude in fractional-flux (i.e. the fraction of starlight blocked by spots), a note whether the rotation period observed by Evryscope is also visible in the TESS light curve (choices are yes for yes, no for no, harm. for a harmonic period, prob. for a likely but noisy match, long for too long to observe in TESS), the TESS-measured starspot amplitude in ΔM_{TESS} , the TESS-measured starspot double-amplitude in fractional-flux (i.e. the fraction of starlight blocked by spots), the estimated starspot temperature in K, the Evryscope-measured starspot coverage fraction, the estimated stellar mass in M_{sol} , the estimated stellar radius in R_{sol} , the estimated stellar effective temperature in K, and the estimated spectral type.

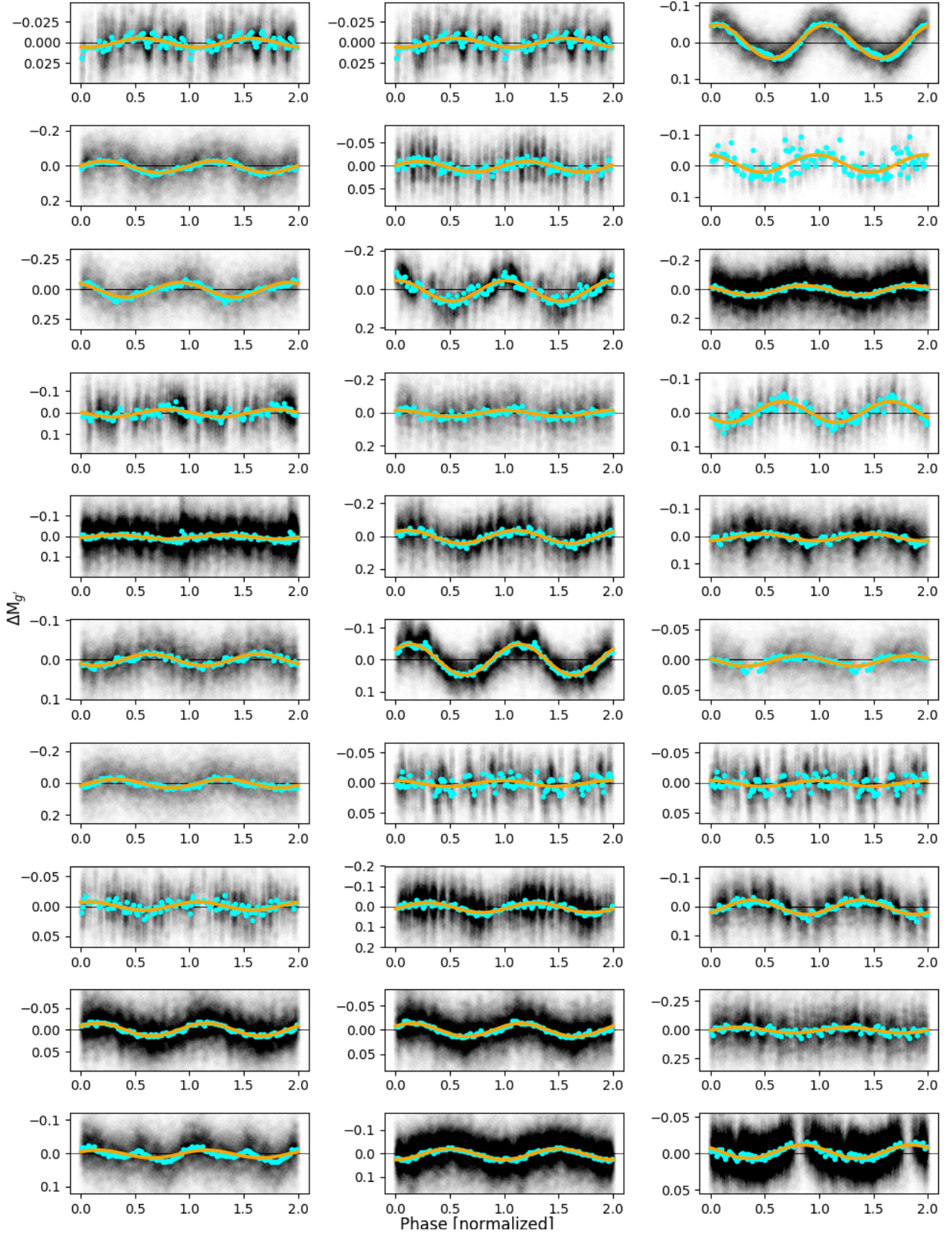


Figure 2. A random subset of all photometric rotation periods found in Evryscope light curves for 113 cool flare stars. In each panel, we plot $\Delta M_{g'}$ magnitudes versus phase. We repeat the phased epochs twice to better display the periodicity. A phased and binned Evryscope light curve is overlaid (in blue), along with a best-sinusoid fit to the unbinned data (in orange). We sometimes detect periods with additional periodicity at harmonics of the strongest peak, such as in the bottom-left panel.

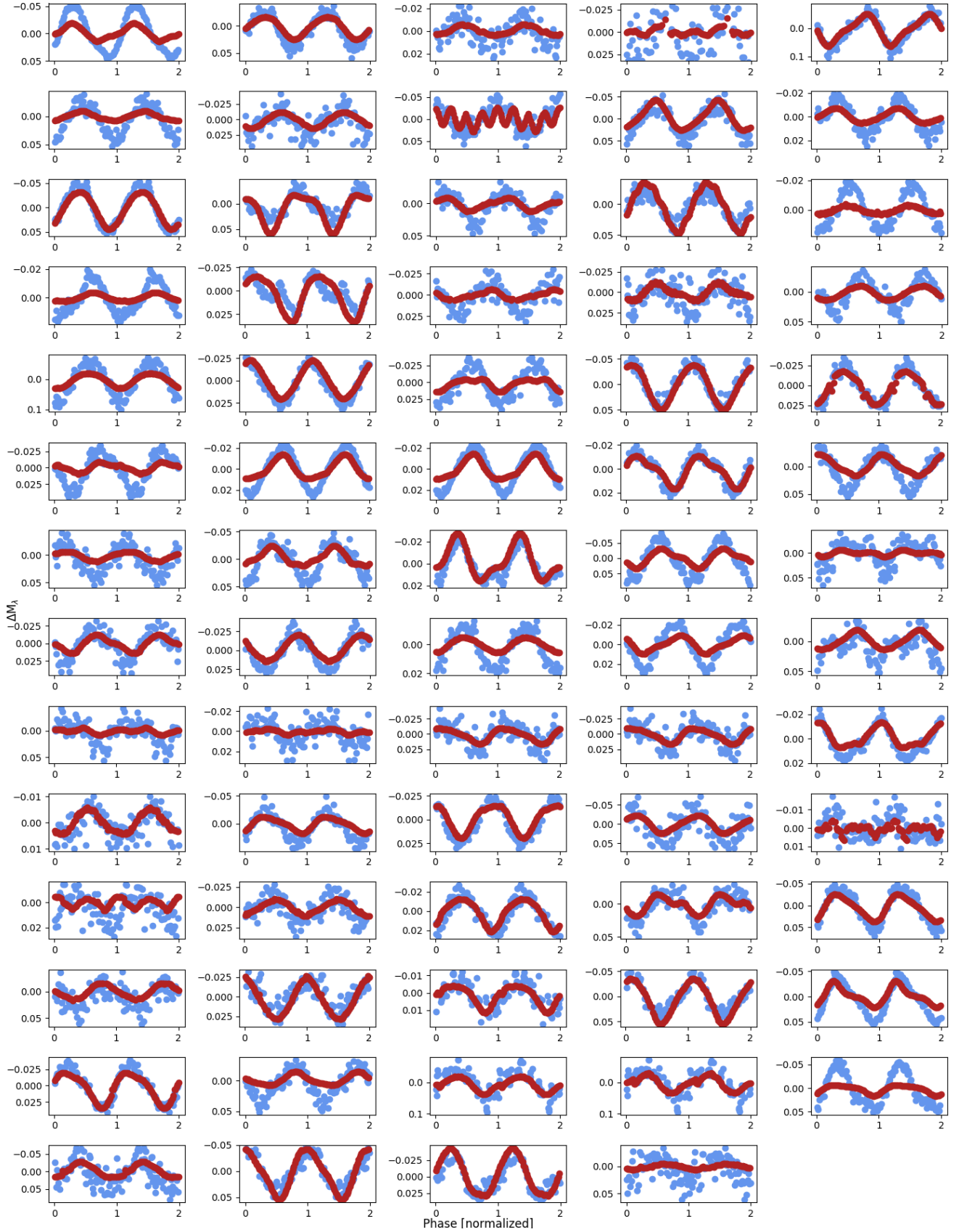


Figure 3. Phased and binned light curves of all 69 cool rotators for which the TESS light curve folds up exactly to the Evryscope-detected period. The phased and binned Evryscope (blue) and TESS (red) light curves are overlaid. In each panel, we plot the normalized flux $\Delta F/F$ versus phase. We repeat the phased epochs twice to better display the periodicity. We find the amplitudes of the TESS light curves are almost universally less than or equal to the Evryscope amplitudes. We note the increase in spot contrast in the blue g' bandpass versus the red T bandpass. From visual inspection and K-S tests, this color difference does not strongly correlate with the stellar effective temperature of our K5-M4 stars or with the presence of companion stars in the TESS pixel, which is 4X larger.

by Shibata et al. (2013); Notsu et al. (2019) as:

$$E_{\text{flare}} = \frac{B^2}{8\pi} A_{\text{Spot}}^{3/2} \quad (3)$$

B is the surface magnetic field strength, and A_{Spot} is the smallest spot group area that could release a flare of energy E_{flare} . We note that true spot sizes could be at least an order of magnitude larger than those given by this very simplified model. We therefore plot the largest flares we observed from each star as a function of the estimated starspot coverage of that star in Figure 6. We then overlay lines of minimum starspot coverage capable of generating the maximum-observed flare energy from each star, for representative magnetic field strengths of 0.5 kG, 1 kG, and 2 kG as shown in Figure 6. Because the true spot coverage ought to lie to the right of this line (i.e. greater spot coverage), we may constrain the minimum field strength B associated with our starspots (in certain line-of-sight spot geometries, a smaller field could be several kG larger).

We find most stars in our sample lie to the right of the 0.5 kG field line, and all stars lie to the right of the 2 kG line. We therefore find a minimum magnetic field of 0.5 kG and a largest value for the minimum field strength of several kG, in broad agreement with previous measurements of the magnetic strengths of cool stars (Shulyak et al. (2017) and references therein). Interestingly, these field strengths are smaller than but comparable to those measured for rotating solar-type stars by Notsu et al. (2019). We also note that Figure 6 shows a gradient in stellar mass across the plane of spot coverage versus maximum flare energy, implying late-type stars may sometimes have a smaller minimum field strength than earlier-type stars.

3.3. Flaring and stellar rotation

Astudillo-Defru et al. (2017) and Newton et al. (2017) explore an increase in stellar activity as a function of rotation until the increase in activity shows saturation at periods shorter than ~ 10 days. For those stars in our sample with recovered flares, we compare the amplitudes, energies and frequencies of their flares as a function of stellar rotation.

3.3.1. Statistics of fast and slow rotators

We find an apparent increase in flare energy, amplitude, and superflare occurrence at short rotation periods, in general agreement with earlier results (e.g. Maehara et al. (2012); Paudel et al. (2018); Davenport et al. (2019)). However, some previous superflare surveys do not find any correlation of flare energy with rotation period, e.g. (Maehara et al. 2012; Günther et al. 2019). Maehara et al. (2012) suggest the maximum energy of a flare is thought to be dependent on the stored energy of a local active region, which does not necessarily depend on the stellar rotation. More recently, Davenport et al. (2019) do find that flare strength decreases with rotation period for all slowly-rotating cool stars. We note Günther et al. (2019) studied short-period rotators and Maehara et al. (2012) studied solar-type superflare stars instead of cool stars.

The relative difficulty in recovering long rotation periods means we may be sampling all activity levels at short

periods and only the most common activity at long periods. This bias means that we must exercise caution in interpreting our results.

To correct for differences in stellar activity observables as functions of the rotation period, we group all recovered flare stars into <10 day and >10 day period bins of short-period and long-period rotators, respectively. We hypothesize our short-period and long-period rotators are drawn from the same underlying distribution of superflare rates. Because we sample more short-period rotators than long-period rotators, we construct our random distribution of superflare rates based upon the observed distribution of short-period rotators.

We perform a Monte Carlo test of 10,000 trials with the goal of distinguishing if 71 short-period and 42 long-period rotators from the same simulated population can differ as much as our actual rotators do. In each trial, we simulate the same numbers of short-period rotators and long-period rotators as we actually observed, and test how often these simulated rotators differ as much as our observed rotators do by using the SciPy (Jones et al. 2001–) implementation of the two-sided asymptotic Kolmogorov-Smirnov (K-S) statistic (Massey 1951).

All three stellar activity observables easily distinguish between our actual short-period and long-period rotators, with large K-S statistics and small p-values. This suggests they do not come from the same population. The MC trials support this interpretation: the K-S statistic and p-value of simulated rotators randomly drawn from the same underlying population do not distinguish between short and long-periods. Across 10,000 trials, the minimum p-values are 0.18, 0.22 and 0.10 and maximum K-S statistic values are 0.21, 0.20 and 0.23 for the superflare rate, maximum flare energy, and starspot coverage respectively. Since the simulated rotators cannot reproduce the large difference in the activity of our actual rotators, we conclude the difference between our actual short-period and long-period rotators is unlikely to be due to sample bias. These results are displayed in Table 2.

3.3.2. Flare stars in the mass-rotation plane

To investigate the activity of our flare stars throughout spin-down, we plot them in the mass-rotation plane and compare against rotators from other surveys. We plot low-mass and long-period rotators from the MEarth survey Newton et al. (2018), and early M-dwarf to late K-dwarf rotators from the KELT survey Oelkers et al. (2018) in Figure 8. We convert the stellar effective temperatures from Oelkers et al. (2018) to stellar masses using the relations given in Table 5 in the Appendix of Kraus & Hillenbrand (2007). We find that Evryscope flare stars occupy a similar parameter-space in the mass-rotation plane as these surveys, but extend to longer rotation periods than the sources from KELT. Our sample does not reach masses as low as many of those observed by MEarth.

In the left three panels of Figure 9, we explore the mass and rotation period as functions of the starspot coverage fraction, maximum flare energy observed from each star and the superflare rate of each star. We find the superflare rate decreases with longer rotation periods and decreases for higher mass, and that the maximum energy from the stars decreases for lower stellar mass and with

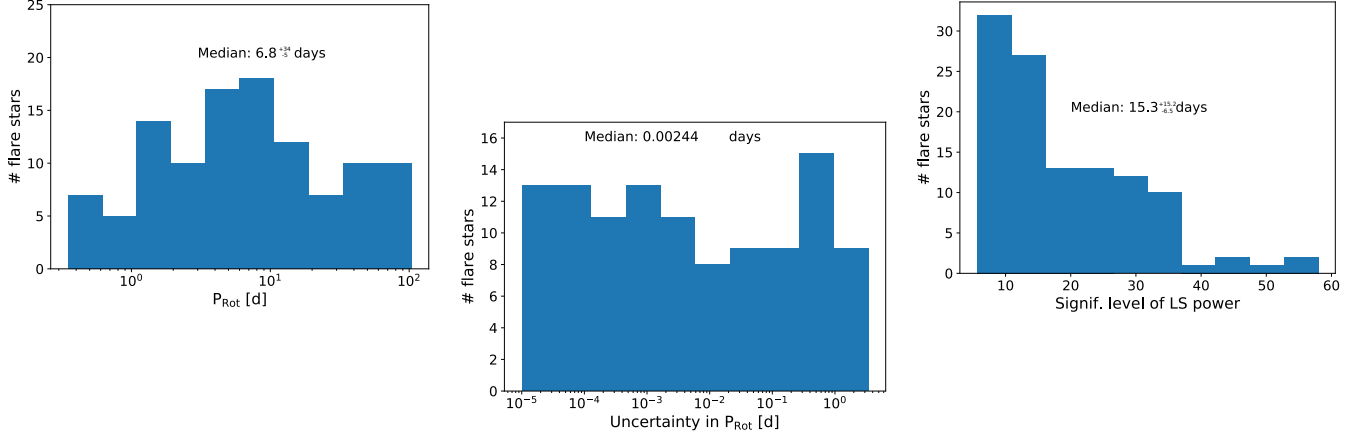


Figure 4. Left panel: Histogram of the distribution in cool flare star periods detected by Evryscope, with a median period and 1σ spread in the distribution of periods of 6.8^{+34}_{-5} days. Middle panel: Histogram of the distribution of the Evryscope period uncertainties, with a median uncertainty in detected period and 1σ spread in the distribution of period uncertainties of $0.00244^{+0.4}_{-0.00239}$ days. Right panel: Histogram of the distribution in LS power, with a median significance of detection and 1σ spread in the distribution of LS significance of 15.3^{+15}_{-6} .

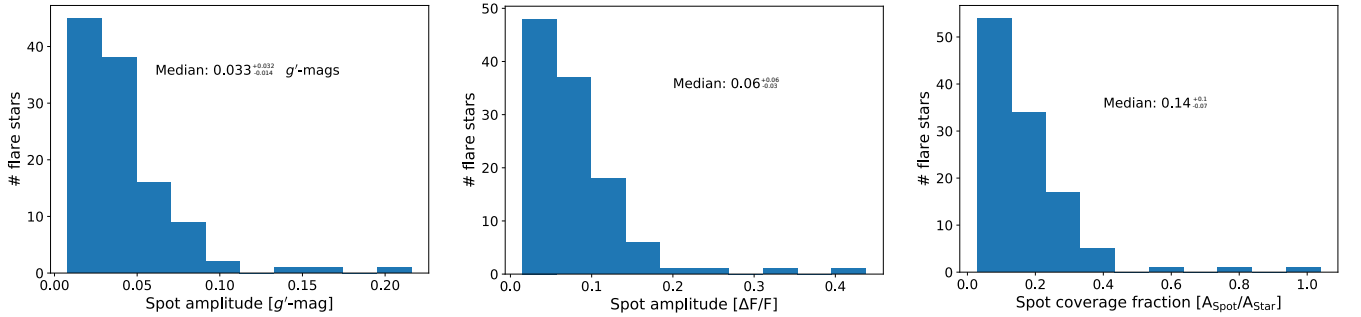


Figure 5. Left panel: Histogram of the distribution of rotation period amplitude of oscillation in cool flare star periods detected by Evryscope, with a median amplitude and 1σ spread in the distribution of amplitudes of $0.033^{+0.032}_{-0.014}$ g' magnitudes. Middle panel: Same as left panel, except in normalized flux units $\Delta F/F$, or the fraction of light blocked by spots, with a median amplitude and 1σ spread in the distribution of normalized flux amplitudes of $0.061^{+0.061}_{-0.026}$. Right panel: Histogram of the distribution in starspot coverage fraction, with a median significance of detection and 1σ spread in the distribution of spot coverage fraction of $0.14^{+0.12}_{-0.07}$.

longer rotation periods. Starspot coverage decreases with longer rotation periods and increases for lower masses. A possible brief rise in the starspot coverage is apparent to the eye at intermediate periods.

3.3.3. Flare stars in the mass-Rossby plane

In addition to the rotation period, stellar rotation is also quantified by the Rossby number: $R_o = P_{\text{Rot}}/\tau_{\text{Conv}}$, where τ_{Conv} is the convective turnover timescale in the star. R_o gives the relative strength of Coriolis forces

and inertial forces in the star (i.e. when the Rossby number is small, the star rotates quickly, and Coriolis forces have the greatest impact upon the surface magnetic field). Convective turnover time is calculated using Equation 11 of Wright et al. (2011). This equation is valid in the mass range $0.09 < M_{\text{Star}}/M_{\odot} < 1.36$. Because the convection turnover time depends upon the stellar mass, inaccuracy in the determination of the mass used in calculating convection turnover timescale will be propagated to the Rossby number. In the cool star mass

Table 2
Stellar activity of short period ($P_{\text{Rot}} < 10$ d) vs. long period ($P_{\text{Rot}} > 10$ d) rotators

Stellar activity observable	p_{obs}	K-S _{obs}	Fraction trials $p_{\text{sim}} < p_{\text{obs}}$	p_{trials} minimum value	Fraction trials K-S _{sim} > K-S _{obs}	K-S _{trials} maximum value
Superflare rate	7.3×10^{-5}	0.43	$< 10^{-4}$	0.18	$< 10^{-4}$	0.21
Largest flare energy	1.2×10^{-6}	0.51	$< 10^{-4}$	0.22	$< 10^{-4}$	0.20
Spot coverage	0.0097	0.31	$< 10^{-4}$	0.10	$< 10^{-4}$	0.23

Notes. We perform K-S tests on the stellar activity of our 71 short-period ($P_{\text{Rot}} < 10$ d) and 42 long-period ($P_{\text{Rot}} > 10$ d) rotators to distinguish if they arise from two distinct populations. We observe higher superflare rates, maximum flare energies, and starspot coverage from short-period rotators than long-period ones. While short-period and long-period rotators have distinct activity levels to significant p-values, we perform MC tests of 10K trials each to ensure our results are not entirely dependent on the larger number of short-period rotators. In each trial, we simulate the distribution of short-period rotators using acceptance-rejection sampling and draw the number of short-period and long period rotators we observed. We find that the fraction of the trials in which the K-S statistic and p-value of our simulated rotators more strongly distinguishes between short and long-periods than do the K-S statistic and p-value of our actual rotators is essentially zero. Across 10K trials, the minimum p-values are 0.18, 0.22 and 0.10 and the largest K-S statistic values are 0.21, 0.20 and 0.23 for the superflare rate, maximum flare energy, and starspot coverage respectively. The p-values of the observed rotators are more than an order of magnitude better, and the K-S statistic values of the observed rotators are twice as high.

Table 3
Stellar activity of fast ($R_o < 0.04$), intermediate ($0.04 < R_o < 0.4$), and slow ($R_o > 0.44$) rotators

Stellar activity observable	Fast vs. intermediate p_{obs}	Fast vs. intermediate K-S _{obs}	Intermediate vs. slow p_{obs}	Intermediate vs. slow K-S _{obs}
Superflare rate	0.53	0.19	0.00014	0.466
Largest flare energy	0.39	0.21	0.076	0.27
Spot coverage	0.21	0.25	0.0012	0.41

Notes. We perform K-S tests on the stellar activity observables of our 25 fast rotators ($R_o < 0.04$), 55 intermediate-period rotators ($0.04 < R_o < 0.4$), and 33 slow rotators ($R_o > 0.44$) to distinguish if they arise from distinct populations. We do not observe significant K-S statistic values or p-values between the stellar activity of our fast and intermediate rotators. We do observe a significant difference between the superflare rate and starspot coverage of the intermediate and slow rotators. The largest flare energies of the intermediate and slow rotators do not demonstrate significant differences, likely due to the small numbers of flare stars observed since the binned flares in Table 2 do display a difference. We note that we do not confirm the higher activity of intermediate rotators detected in MEarth light curves by Mondrik et al. (2019). We believe this to be a result of our sample size and urge future work with larger samples of cool stars.

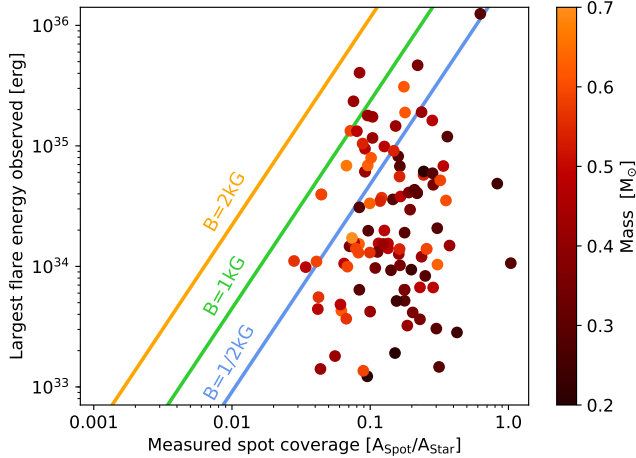


Figure 6. Measured starspot coverage of each rotating star versus the maximum-observed flare energy from that star. Scaling relations for the minimum spot coverage needed to generate flares at the observed energies are overlaid for representative field strengths of 0.5 kG, 1 kG, and 2 kG. For each scaling relation for a particular field strength, the measured spot coverage should lie to the right of that line. We find most of our rotators lie to the right of the 0.5 kG field line, and all lie to the right of the 2 kG line, placing upper limits on the minimum field strength of our sample. We also color-code each data point representing a rotating flare star by its stellar mass, finding a gradient in flare energy between early and mid M-dwarf stars.

range, uncertainty in the stellar mass of $0.1 M_{\odot}$ can propagate to errors in the Rossby number of up to ~ 0.15 dex.

We find 25 (22.1%) of our flare stars to be fast rotators ($R_o < 0.04$), 55 (48.7%) to be intermediate-period rotators ($0.04 < R_o < 0.4$) undergoing rapid evolution to the topology of the surface magnetic field during spin-down, and 33 (29.2%) to be slow rotators ($R_o > 0.44$). We define fast, intermediate, and slow rotators using the convention of Mondrik et al. (2019). In the right three panels of Figure 9, we explore the mass and Rossby number as functions of the maximum flare energy observed from each star and the superflare rate of each star. We find our flare star sample explores the period-gap reported in earlier works (e.g. Newton et al. 2018) during spin-down due to the slow spin-down process of the early field M-dwarfs we most frequently observe.

We note the lack of saturated rotators. We originally searched for rotators with periods greater than 1.25 days and only re-computed LS periodograms down to 0.1 days within our sample of 113 rotating stars, excluding several potential activity-saturated rotators from the current work. This results in the larger numbers of intermediate than fast rotators we report above, but does not imply that we report a higher astrophysical rate of intermediate to saturated rotators. Wright et al. (2011) gives the rotation periods corresponding to low Rossby number, saturated-activity fast rotators (i.e. $R_o < 1$) in the cool star mass range as 0.58 to 1.22 days. We therefore observe an increase in the density of rotators

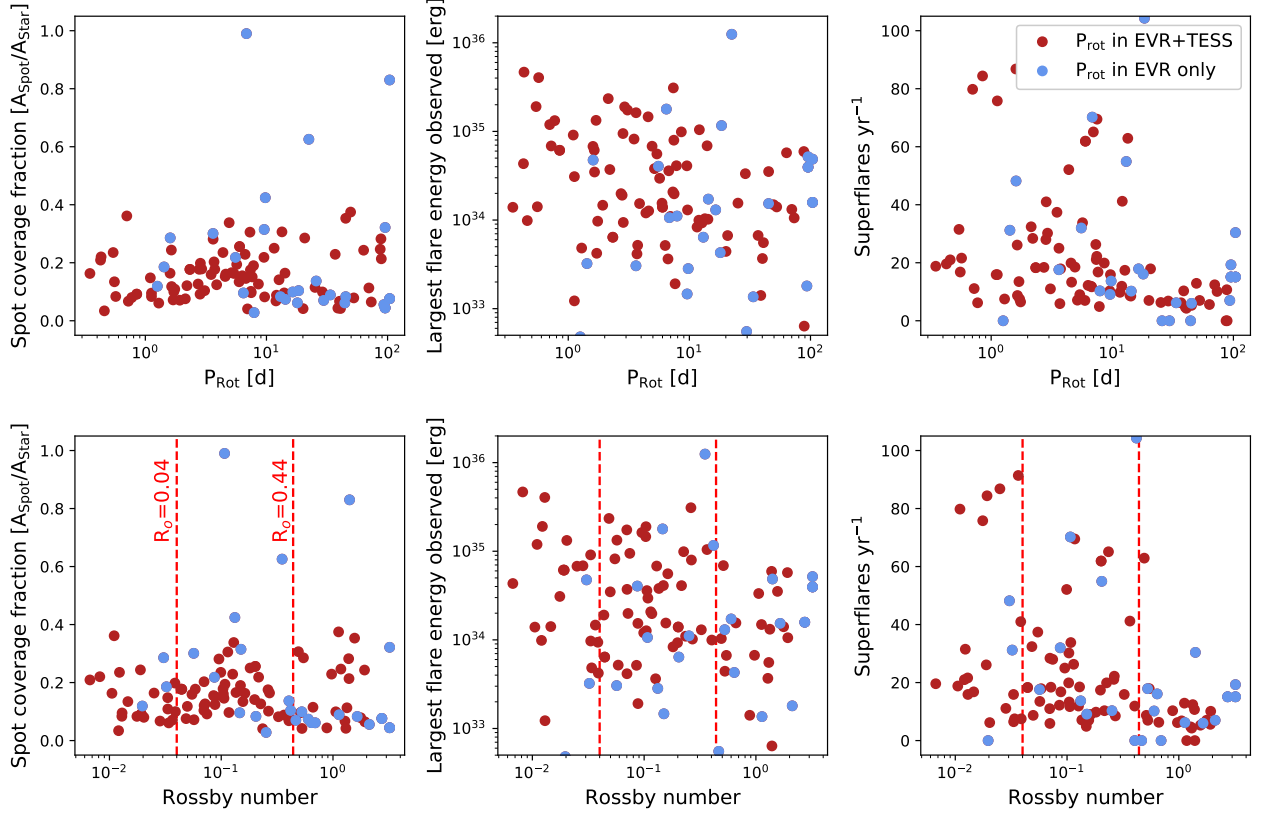


Figure 7. Stellar activity observables as functions of stellar rotation and Rossby number. Red dots have periods confirmed in both Evryscope and TESS light curves; blue dots have periods only from Evryscope. We consider the red periods to be the highest-quality. Top panels: The starspot coverage fraction, largest observed flare energy from each star, and superflare rate versus rotation period. All three types of activity decrease at longer rotation periods, as described by Table 2 and Table 3. However, an apparent pile-up in high spot coverage is visible to the eye at periods of ~ 5 days. Bottom panels: The starspot coverage fraction, largest observed flare energy from each star, and superflare rate versus Rossby number. Vertical red dashed lines indicate the boundaries between the Rossby numbers of fast, intermediate, slow rotators. All three types of activity decrease at longer rotation periods, as described by Table 2 and Table 3. However, an apparent pile-up in high spot coverage is visible to the eye at intermediate Rossby numbers. With so few rotators in our sample, the pile-up is not detected in the K-S tests of Table 3. If real, this tentative evidence for changing surface magnetic field geometry during spin down may correlate with the increased activity of Mondrik et al. (2019).

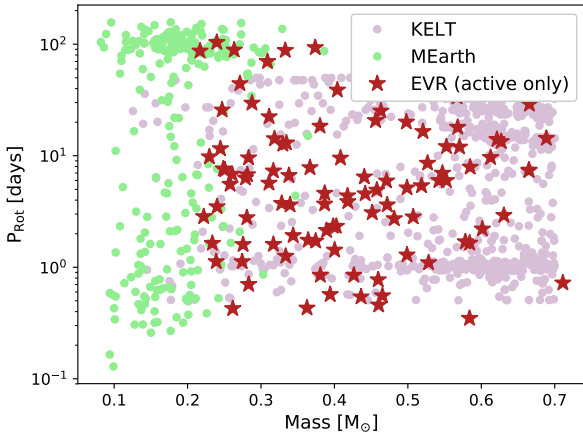


Figure 8. Evryscope cool flare stars in the mass-rotation plane, compared to rotating cool stars from MEarth and KELT (e.g Newton et al. (2018), Oelkers et al. (2018)). We observe a similar distribution in our flare stars compared to these other surveys, but we explore a broader period range for early M-dwarfs and late K-dwarfs.

at Rossby numbers approaching saturation but observe few saturated rotators at $R_o < 0.02$ in our sample due to our initial cut in the period search-range. We also check that the large numbers of intermediate rotators and few fast saturated rotators is not a result of unexpected large errors in calculating the convection turnover time. Because our typical uncertainty in stellar mass is $\sim 0.1\text{--}0.2M_\odot$ (i.e. a few spectral sub-types) can lead to errors in the Rossby number of up to 0.2–0.3 dex, our uncertainties are unlikely to account for the nearly order-of-magnitude difference necessary to move data-points between the intermediate rotator and saturated rotator regime (visible as the bottom gray sequence in the bottom two panels of Figure 9).

3.3.4. Inconclusive increased activity of intermediate rotators

We divide up all 113 rotating flare stars into fast, intermediate, and slow rotators and test if the stellar activity of the intermediate rotators is from a different population than the stellar activity of the fast and slow rotators. We perform 2-sample KS tests as described in Section 3.3.1 separately for the starspot coverage, superflare rate, and maximum flare energy. We limit our hypothesis test-

ing to three observables to avoid searching for random correlations. We choose observables that probe a broad range of stellar activity: a flare rate, a flare size, and the extensiveness of the active regions that emit flares.

For each observable, we test whether the fast and intermediate rotators come from the same population, and we test whether the intermediate and slow rotators come from the same underlying population. We observe a general decrease in activity with decreasing rotation, in agreement with Table 2 and earlier studies (e.g. Newton et al. (2017); Davenport et al. (2019); Ilin et al. (2019)). However, we do not confirm the increased activity of intermediate rotators reported by Mondrik et al. (2019). This is likely due to the small number of flare stars we observe; we urge more extensive studies of rotating flare stars be made. These results are displayed in Table 3.

3.4. TESS vs. Evryscope sinusoidal amplitudes

While folding the high-cadence TESS light curves of each rotator to the Evryscope period as described in Section 2.3, we noticed the Evryscope sinusoidal amplitudes are consistently greater than or equal to those in TESS. We are unsure why our spots are sometimes (but not always) so high-contrast in the blue compared to the red. We compute the normalized fractional flux difference between Evryscope and TESS amplitudes for our 69 exact period-matches of Section 3.3.1, for a median flux difference and 1σ spread in the distribution of flux difference of $0.036^{+0.025}_{-0.021}$. It is likely this is an effect of the differing blackbody temperatures of the spot and star. We hypothesized the rotators with the greatest amplitude differences should correlate with stellar effective temperature and therefore color. We checked the correlation visually and observed no trend; we also performed a two-sample K-S test on the flux differences of early and late rotators, and found no correlation ($p=0.21$). We then hypothesized the 4X larger TESS pixels capture more flux from companion stars, diluting the amplitude. We checked the number of Gaia DR2 sources for each star, and found the larger flux differences in amplitude also do not correlate with more companion stars ($p=0.45$). We find between 1 and 17 Gaia DR2 sources per $21''$ aperture; 94% of our 69 targets have fewer than four nearby sources and display no trend versus difference in flux amplitude. Although not statistically significant, the remaining 6% of the targets with four or more sources do display low flux amplitude differences. Future work is needed to ascertain how the spot blackbody relates to the flux amplitude differences.

4. DISCUSSION AND CONCLUSIONS

We observe 113 rotators in our sample of 284 late K and early-to-mid M flare stars, with periods ranging from 0.3487 to 104 days. We observe rotation periods of stars throughout the spin-down process.

We compute the Rossby number of each rotator and observe 25 fast rotators ($R_o < 0.04$) with saturated activity, 55 intermediate-period rotators ($0.04 < R_o < 0.4$) undergoing probable changes to the surface magnetic field, and 33 slow rotators ($R_o > 0.44$).

This sample of rotating flare stars was investigated as a subset of the ongoing Evryscope survey of all bright nearby stars; we selected these 284 flare stars because

they were observed in the first quarter of TESS observations and had 2-minute cadence light curves in the blue (Evryscope) and in the red (TESS), allowing future study of stellar activity in both bands. TESS observes most stars for 28 days, limiting the precision of rotation periods with $P_{rot} > 1$ day where early M-dwarf rotation periods and HZ planet orbits coincide. We measure small period uncertainties due to the long observation time of Evryscope, with a median observed period of 6.8 days and a median period uncertainty of 0.0024 days. We find the sinusoidal amplitudes of rotation of our cool stars often exceed 1% variability. We observe amplitudes from 0.008 to 0.216 g' magnitudes, suggesting long-term, moderate-precision ground based observations may greatly increase the number and precision of rotation period measurements for nearby cool stars.

We fold the 2-minute cadence TESS light curve of each star to the Evryscope-detected period. We find the sinusoidal amplitude of rotation in the red TESS-bandpass is less than or equal to that in the blue Evryscope bandpass. This could imply spots have higher contrast against the star in the blue or possibly that the 4X-larger TESS pixels have a higher rate of stellar crowding. We do not see evidence this trend is a result of changing stellar effective temperature.

Using the sinusoidal amplitude of rotation, we compute the minimum fraction of the stellar hemisphere covered by starspots. We measure a median spot coverage of 14% of the stellar hemisphere. We predict the largest flares these spots could emit for several values of the stellar magnetic field strength and subsequently compare these large predicted flares against the largest flares we actually observed. We find stellar magnetic fields of at least 500 G are most-consistent with our observed flares and spots. The minimum field strength of the later-type cool stars exhibits a broader spread in values than the minimum field strength of the earlier-type cool stars.

We find our $P_{Rot} < 10$ d rotators demonstrate higher superflare rates, largest flare energies observed per star, and starspot coverage fractions than do $P_{Rot} > 10$ d rotators, at p -values of 7.3×10^{-5} , 1.2×10^{-6} and 0.0097, respectively. Therefore, we do not conclusively confirm the increased activity of intermediate rotators seen in previous studies. A possible change to starspot coverage is observed at intermediate rotation periods. Due to our small sample size, this apparent change is not recovered at a significant level by K-S tests. We suggest future work in larger samples of intermediate rotators be performed to confirm this apparent change to starspot coverage during spin-down.

ACKNOWLEDGEMENTS

WH, HC, NL, JR, and AG acknowledge funding support by the National Science Foundation CAREER grant 1555175, and the Research Corporation Scialog grants 23782 and 23822. HC is supported by the National Science Foundation Graduate Research Fellowship under Grant No. DGE-1144081. OF and DdS acknowledge support by the Spanish Ministerio de Economía y Competitividad (MINECO/FEDER, UE) under grants AYA2013-47447-C3-1-P, AYA2016-76012-C3-1-P, MDM-2014-0369 of ICCUB (Unidad de Excelencia ‘María de Maeztu’). The Evryscope was constructed under National Science Foundation/ATI grant AST-1407589.

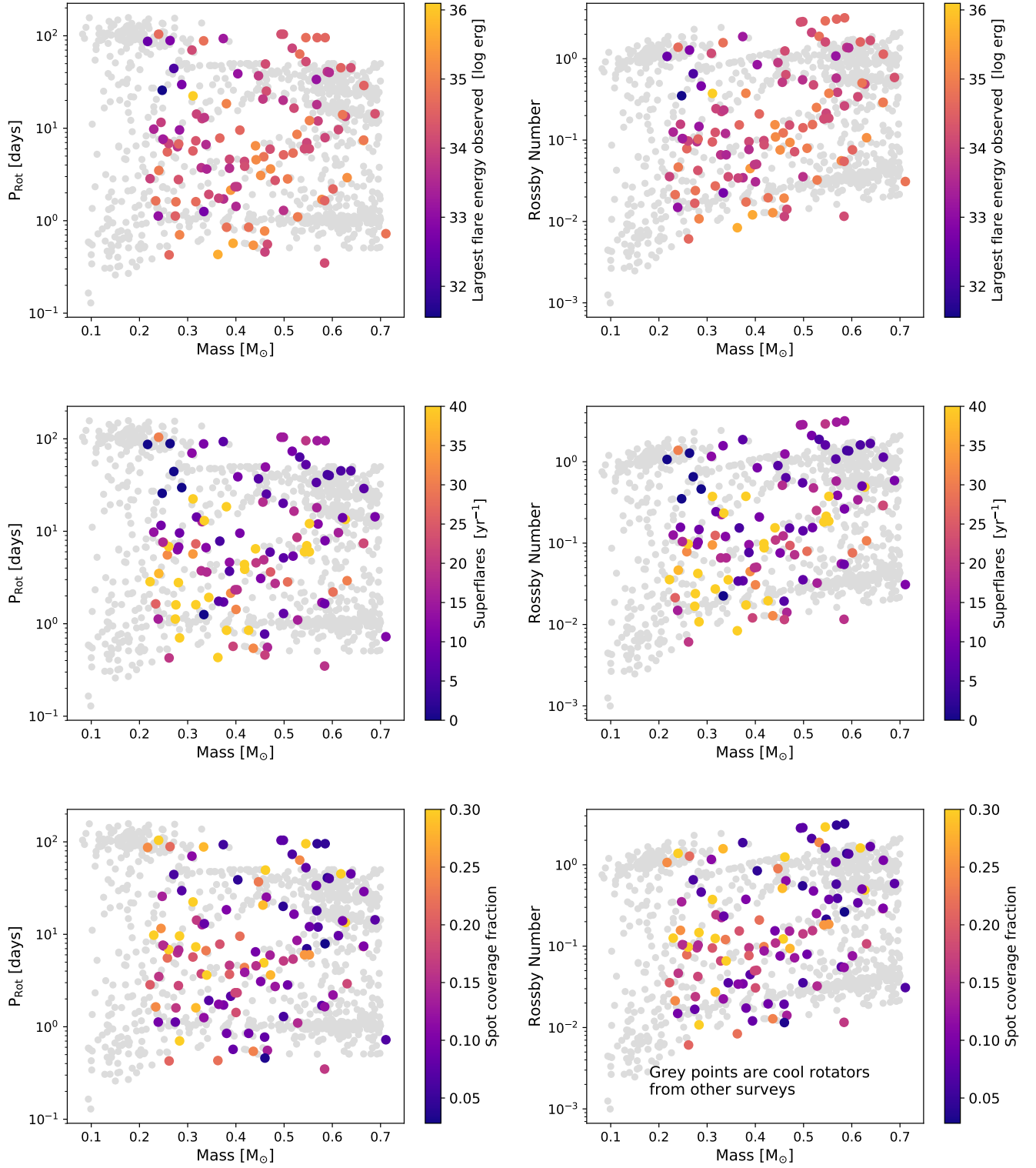


Figure 9. Left panels: Evryscope flare stars in the mass-rotation plane. Flare stars are scaled in color by (top panel to bottom) the maximum flare energy observed per star, superflare rate, and spot coverage, respectively. MEarth and KELT rotators are plotted in grey for reference. Right panels: Evryscope flare stars in the mass-Rossby number plane, with coloring the same as on the left. Evryscope flare stars explore the spin down transition region from fast to slow rotation where Mondrik et al. (2019) report increased flaring.

This paper includes data collected by the TESS mission. Funding for the TESS mission is provided by the NASA Explorer Program.

This work has made use of data from the European Space Agency (ESA) mission *Gaia* (<https://www.cosmos.esa.int/gaia>), processed by the *Gaia* Data Processing and Analysis Consortium (DPAC, <https://www.cosmos.esa.int/web/gaia/dpac/consortium>). Funding for the DPAC has been provided by national institutions, in particular the institutions participating in the *Gaia* Multilateral Agreement. This research made use of Astropy,³ a community-developed core Python package for Astronomy (Astropy Collaboration et al. 2013; Price-Whelan et al. 2018), and the NumPy, SciPy, and Matplotlib Python modules (van der Walt et al. 2011; Jones et al. 2001; Hunter 2007).

Facilities: CTIO:Evryscope, TESS

REFERENCES

- Affer, L., Micela, G., Favata, F., & Flaccomio, E. 2012, *MNRAS*, 424, 11
- Airapetian, V. S., & Usmanov, A. V. 2016, *ApJ*, 817, L24
- Alvarado-Gómez, J. D., Drake, J. J., Cohen, O., Moschou, S. P., & Garraffo, C. 2018, *ApJ*, 862, 93
- Ambartsumian, V. A., & Mirzoian, L. V. 1975, in *IAU Symposium*, Vol. 67, *Variable Stars and Stellar Evolution*, ed. V. E. Sherwood & L. Plaut, 3–14
- Astropy Collaboration, Robitaille, T. P., Tollerud, E. J., et al. 2013, *A&A*, 558, A33
- Astudillo-Defru, N., Delfosse, X., Bonfils, X., et al. 2017, *A&A*, 600, A13
- Baliunas, S., Sokoloff, D., & Soon, W. 1996, *ApJ*, 457, L99
- Berdugina, S. V. 2005, *Living Reviews in Solar Physics*, 2, 8
- Berta, Z. K., Irwin, J., Charbonneau, D., Burke, C. J., & Falco, E. E. 2012, *AJ*, 144, 145
- Borucki, W. J., Koch, D., Basri, G., et al. 2010, *Science*, 327, 977
- Brown, T. M. 2014, *ApJ*, 789, 101
- Cohen, O., Drake, J. J., Gloer, A., et al. 2014, *ApJ*, 790, 57
- Davenport, J. R. A., Covey, K. R., Clarke, R. W., et al. 2019, *ApJ*, 871, 241
- Dressing, C. D., & Charbonneau, D. 2015, *ApJ*, 807, 45
- Gaia* Collaboration, Prusti, T., de Bruijne, J. H. J., et al. 2016, *A&A*, 595, A1
- Gaia* Collaboration, Brown, A. G. A., Vallenari, A., et al. 2018, *A&A*, 616, A1
- Garraffo, C., Drake, J. J., & Cohen, O. 2015, *ApJ*, 813, 40
- . 2016, *A&A*, 595, A110
- Garraffo, C., Drake, J. J., Dotter, A., et al. 2018, *ApJ*, 862, 90
- Giles, H. A. C., Collier Cameron, A., & Haywood, R. D. 2017, *MNRAS*, 472, 1618
- Günther, M. N., Zhan, Z., Seager, S., et al. 2019, *arXiv e-prints*, arXiv:1901.00443
- Hartman, J. D., Bakos, G. Á., Noyes, R. W., et al. 2011, *AJ*, 141, 166
- Henden, A. A., Templeton, M., Terrell, D., et al. 2016, *VizieR Online Data Catalog*, 2336
- Howard, W. S., Corbett, H., Law, N. M., et al. 2019, *arXiv e-prints*, arXiv:1904.10421
- Hunter, J. D. 2007, *Computing in Science & Engineering*, 9, 90
- Ilin, E., Schmidt, S. J., Davenport, J. R. A., & Strassmeier, K. G. 2019, *A&A*, 622, A133
- Jones, E., Oliphant, T., Peterson, P., et al. 2001–, *SciPy: Open source scientific tools for Python*, [Online; accessed {today}]
- . 2001, *SciPy: Open source scientific tools for Python*
- Kawaler, S. D. 1988, *ApJ*, 333, 236
- Kopparapu, R. K. 2013, *ApJ*, 767, L8
- Kraus, A. L., & Hillenbrand, L. A. 2007, *AJ*, 134, 2340
- Law, N. M., Fors, O., Ratzloff, J., et al. 2016, in *Proc. SPIE*, Vol. 9906, *Ground-based and Airborne Telescopes VI*, 99061M
- Law, N. M., Fors, O., Ratzloff, J., et al. 2015, *PASP*, 127, 234
- Lomb, N. R. 1976, *Ap&SS*, 39, 447
- Maehara, H., Shibayama, T., Notsu, S., et al. 2012, *Nature*, 485, 478
- Mann, A. W., Feiden, G. A., Gaidos, E., Boyajian, T., & von Braun, K. 2015, *ApJ*, 804, 64
- Massey, F. J. J. 1951, *Journal of the American Statistical Association*, 46, 68
- McQuillan, A., Mazeh, T., & Aigrain, S. 2014, *ApJS*, 211, 24
- Mondrik, N., Newton, E., Charbonneau, D., & Irwin, J. 2019, *ApJ*, 870, 10
- Morris, B. M., Curtis, J. L., Sakari, C., Hawley, S. L., & Agol, E. 2019, *arXiv e-prints*, arXiv:1907.00423
- Neff, J. E., O’Neal, D., & Saar, S. H. 1995, *ApJ*, 452, 879
- Newton, E. R., Irwin, J., Charbonneau, D., et al. 2017, *ApJ*, 834, 85
- Newton, E. R., Irwin, J., Charbonneau, D., Berta-Thompson, Z. K., & Dittmann, J. A. 2016a, *ApJ*, 821, L19
- Newton, E. R., Irwin, J., Charbonneau, D., et al. 2016b, *ApJ*, 821, 93
- Newton, E. R., Mondrik, N., Irwin, J., Winters, J. G., & Charbonneau, D. 2018, *AJ*, 156, 217
- Notsu, Y., Shibayama, T., Maehara, H., et al. 2013, *ApJ*, 771, 127
- Notsu, Y., Maehara, H., Honda, S., et al. 2019, *ApJ*, 876, 58
- Nutzman, P., & Charbonneau, D. 2008, *PASP*, 120, 317
- Oelkers, R. J., Rodriguez, J. E., Stassun, K. G., et al. 2018, *AJ*, 155, 39
- O’Neal, D., Neff, J. E., Saar, S. H., & Cuntz, M. 2004, *AJ*, 128, 1802
- Paudel, R. R., Gizis, J. E., Mullan, D. J., et al. 2018, *arXiv e-prints*, arXiv:1812.07631
- Pedregosa, F., Varoquaux, G., Gramfort, A., et al. 2012, *arXiv e-prints*, arXiv:1201.0490
- Pepper, J., Gould, A., & Depoy, D. L. 2003, *ACTAA*, 53, 213
- Pepper, J., Kuhn, R. B., Siverd, R., James, D., & Stassun, K. 2012, *PASP*, 124, 230
- Pepper, J., Pogge, R. W., DePoy, D. L., et al. 2007, *PASP*, 119, 923
- Price-Whelan, A. M., Sipőcz, B. M., Günther, H. M., et al. 2018, *AJ*, 156, 123
- Ratzloff, J. K., Law, N. M., Fors, O., et al. 2019a, *PASP*, 131, 075001
- Ratzloff, J. K., Corbett, H. T., Law, N. M., et al. 2019b, *arXiv e-prints*, arXiv:1905.02738
- Ricker, G. R., Winn, J. N., Vanderspek, R., et al. 2014, in *Proc. SPIE*, Vol. 9143, *Space Telescopes and Instrumentation 2014: Optical, Infrared, and Millimeter Wave*, 914320
- Robertson, P., Mahadevan, S., Endl, M., & Roy, A. 2014, *Science*, 345, 440
- Scargle, J. D. 1982, *ApJ*, 263, 835
- Shibata, K., Isobe, H., Hillier, A., et al. 2013, *PASJ*, 65, 49
- Shulyak, D., Reiners, A., Engeln, A., et al. 2017, *Nature Astronomy*, 1, 0184
- Stassun, K. G., Oelkers, R. J., Paegert, M., et al. 2019, *arXiv e-prints*, arXiv:1905.10694
- Tamuz, O., Mazeh, T., & Zucker, S. 2005, *MNRAS*, 356, 1466
- van der Walt, S., Colbert, S. C., & Varoquaux, G. 2011, *Computing in Science & Engineering*, 13, 22
- Vanderburg, A., Plavchan, P., Johnson, J. A., et al. 2016, *MNRAS*, 459, 3565
- VanderPlas, J. T. 2018, *The Astrophysical Journal Supplement Series*, 236, 16
- Wakeford, H. R., Lewis, N. K., Fowler, J., et al. 2019, *AJ*, 157, 11
- Weber, E. J., & Davis, Leverett, J. 1967, *ApJ*, 148, 217
- Wright, N. J., Drake, J. J., Mamajek, E. E., & Henry, G. W. 2011, *ApJ*, 743, 48
- Yang, H., Liu, J., Gao, Q., et al. 2017, *The Astrophysical Journal*, 849, 36
- Zhan, Z., Günther, M. N., Rappaport, S., et al. 2019, *arXiv e-prints*, arXiv:1903.02061

³ <http://www.astropy.org>